

A Salpeter-like filament linear density function across nearby molecular clouds

Guo-Yin Zhang^{1,*}, Alexander Men'shchikov^{2,*}, Jin-Zeng Li[†]

¹National Astronomical Observatories, Chinese Academy of Sciences, A20 Datun Road, Beijing 100101, China.

²Université Paris-Saclay, Université Paris Cité, CEA, CNRS, AIM, 91191 Gif-sur-Yvette, France.

[†]Guo-Yin Zhang (zgyin@nao.cas.cn) and Alexander Men'shchikov (alexander.menshchikov@cea.fr) contributed equally to this work.

Abstract

Filamentary structures in molecular clouds are thought to play a central role in star formation, yet the statistical distribution of their mass per unit length – and any connection to the stellar initial mass function (IMF) – remains poorly constrained observationally. Here we present a systematic analysis of the filament linear density function (FLDF) across seven nearby molecular clouds spanning ~ 100 – 1000 pc in distance and a wide range of star-forming environments, from quiescent to massive, using the multiscale extraction method *getsf*. The median linear densities of filaments increase approximately linearly with spatial scale, $\bar{\Lambda} \propto Y$, and the fraction of supercritical filaments varies widely among clouds, from a few per cent to over 50%. Only when integrating over the full hierarchy of spatial scales do the combined linear densities across all clouds yield a FLDF that follows a power law $dN/d \log \Lambda \propto \Lambda^{-\alpha}$ with $\alpha \approx 1.30$ – 1.34 , mirroring the Salpeter IMF slope of 1.35 . Our results suggest that the stellar mass spectrum is pre-encoded in the filamentary structure of molecular clouds, providing a direct observational link between the large-scale distribution of interstellar gas and the universal slope of the stellar IMF.

Keywords: Stars: formation, ISM: clouds, ISM: structure, methods: data analysis

Why the stellar initial mass function (IMF) follows a power law $dN/d \log M \propto M^{-1.35}$ at high masses [4], with a slope that appears remarkably universal across diverse star-forming environments [5–7], remains a defining mystery of modern astrophysics [8, 9]. *Herschel* imaging surveys of nearby Galactic clouds have established that dense filaments dominate the mass budget of molecular clouds and host most prestellar cores and star-forming activity [1, 10–12], lending strong support to the filament fragmentation paradigm [13] in

which stars form preferentially within gravitationally unstable filaments. The core mass function (CMF) in nearby molecular clouds closely resembles the stellar IMF [12, 14–17], suggesting that the IMF slope is already imprinted at the stage of dense core formation. If the CMF is set by fragmentation of filaments [18], then the IMF slope may be directly linked to the slope of the filament linear density function (FLDF) – the statistical distribution of filament mass per unit length. Testing this hypothesis requires measuring the FLDF

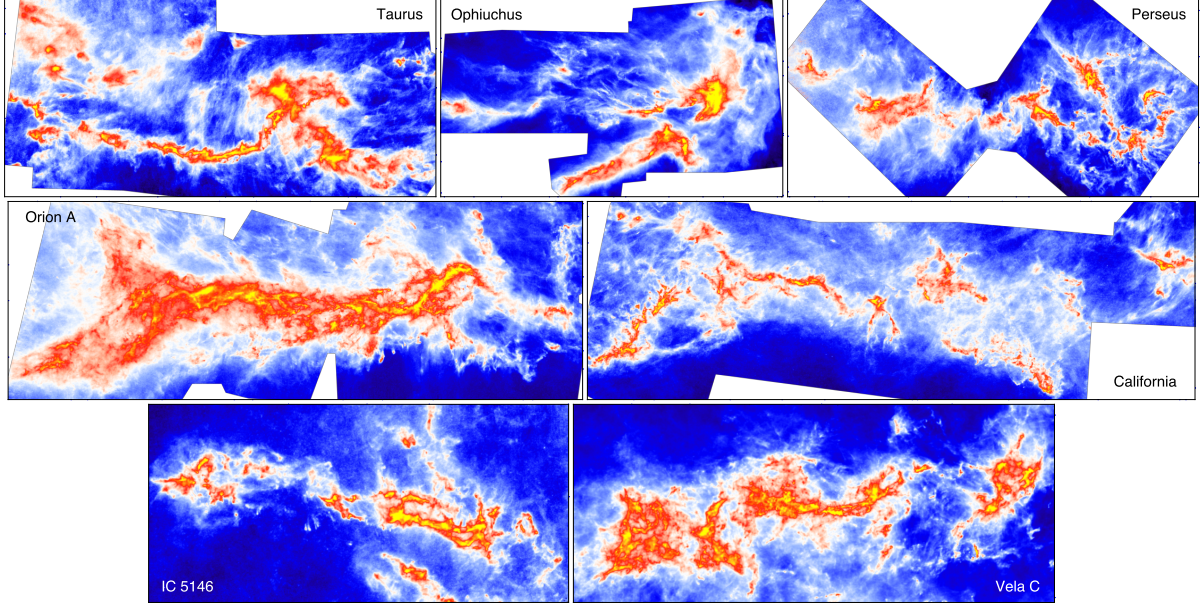


Fig. 1 Overview of the molecular clouds with prominent filamentary structures studied in this work. Shown are high-resolution ($13.5''$) surface density maps derived from *Herschel* PACS and SPIRE images observed in several surveys: HGBS [1] for Taurus, Ophiuchus, Perseus, Orion A, and IC 5146; HOBYS [2] for Vela C; and A-CMC [3] for California.

across a large and diverse sample of molecular clouds.

A key quantity governing filament fragmentation is the linear density Λ (mass per unit length). Filaments exceeding the critical linear density Λ_c are gravitationally unstable and prone to fragmentation into dense cores [19–21]. Observational studies have revealed that filaments are hierarchically substructured, with larger-scale filaments containing intertwined smaller-scale sub-filaments or fibers [22–25], implying that Λ and the FLDF are inherently scale-dependent quantities. The FLDF has been measured in nearby molecular clouds [18, 26], but no systematic study using independent multiscale filament extraction has been undertaken.

Here we present the first measurement of the FLDF across seven nearby molecular clouds – Taurus, Ophiuchus, Perseus, Orion A, California, IC 5146, and Vela C (Fig. 1) – spanning distances of 140–920 pc and a wide range of star formation activity, using the multiscale extraction method *getsf* [27] and the improved profile fitting method of [28]. By combining measurements across all clouds and all spatial scales from 14 to $216''$, we obtain a statistically robust composite FLDF and compare its slope directly with the Salpeter

IMF. The companion paper [29] presents a comprehensive analysis of filament widths, slopes, and volume density profiles across the same sample; the present paper focuses specifically on the statistical distribution of linear densities and its connection to the IMF.

Results

Scale-dependent linear density distributions

Figure 2 presents scale-dependent distributions of the linear densities Λ_k derived from the surface density profiles (equation (2) in Methods), along with the distributions accumulated over all scales. The two bottom rows show differential and cumulative distributions combined over all molecular clouds for improved statistical significance, and include for comparison the distributions derived when averaging filament profiles along entire filament lengths.

Across all molecular clouds, filaments detected on larger scales have progressively higher linear densities. The median values $\tilde{\Lambda}_k$ in the range $[0.07, 3.4] M_\odot \text{pc}^{-1}$ on the $14''$ scale increase to $[3.2, 63] M_\odot \text{pc}^{-1}$ on the $216''$ scale. The relationship between the median linear densities and detection

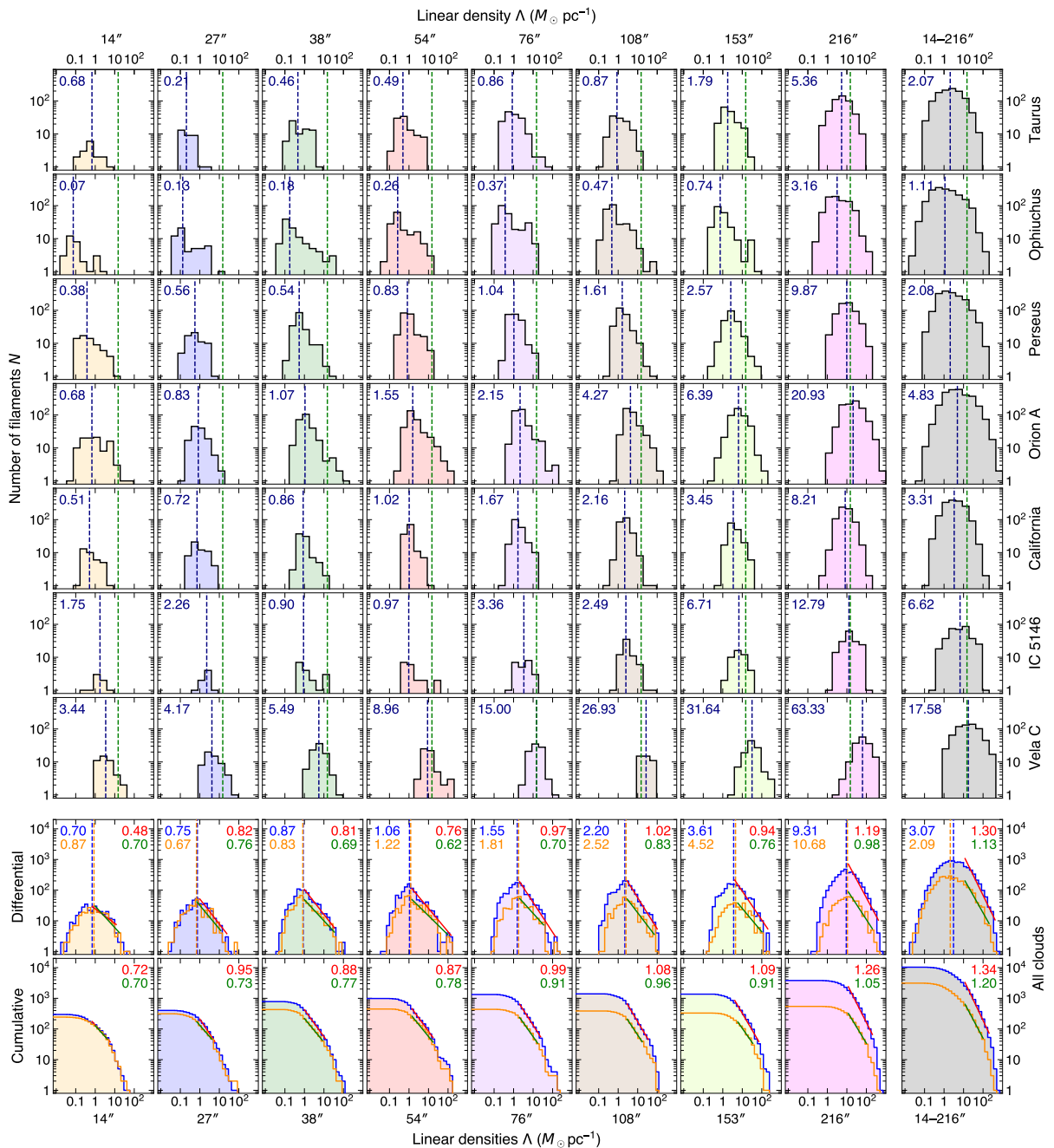


Fig. 2 Scale-dependent distributions of linear densities Λ_k of filaments in the molecular clouds, integrated from surface density profiles. Black and green dashed lines in the seven upper rows indicate median values $\bar{\Lambda}_k$ and the critical value of $15 M_\odot \text{pc}^{-1}$, respectively. The two bottom rows present differential (N) and cumulative (N_C) distributions for filament segments (scale-coloured fills with blue outlines and dashed medians) and entire filaments (orange outlines and dashed medians). Red lines represent power-law fits to the segment distributions above $\bar{\Lambda}_k$, with slopes α_k indicated in red; green lines show the corresponding fits to the entire-filament distributions, with slopes in green; for the all-scales combined panels, fits are performed above the maximum median value on the 216'' scale. Histogram fill colours distinguish detection scales Y_k , following the same colour sequence as in Extended Data Fig. 7; rightmost panels, showing distributions accumulated over all scales, are filled in grey.

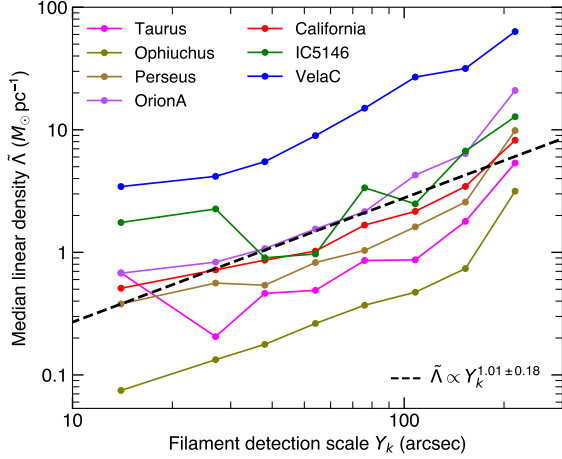


Fig. 3 Median linear density $\tilde{\Lambda}$ of filaments as a function of detection scale Y_k for the seven molecular clouds (coloured lines). The dashed line shows a power-law fit to the combined data, $\tilde{\Lambda} \propto Y_k^{1.01 \pm 0.18}$, indicating that filament linear density increases approximately linearly with detection scale across all clouds. The cloud-to-cloud spread at each scale reflects genuine variation in the overall mass content of the filamentary networks. The steeper rise visible at the two largest scales (153–216 $''$) for most clouds may reflect an increasing contribution of filament envelopes at large detection scales.

scales follows a power law $\tilde{\Lambda} \propto Y_k^{1.01 \pm 0.18}$ (Fig. 3), with the exponent varying in the range [0.72, 1.2] among individual clouds. Vela C shows the highest median linear densities at all scales and Ophiuchus the lowest, reflecting genuine differences in the mass content of their filamentary networks.

We constructed the composite FLDF by combining linear densities of all filament segments from all seven molecular clouds and all eight spatial scales. Our tests with power-law model distributions $dN/d \log \Lambda \propto \Lambda^{-\alpha}$ demonstrate that the slope α derived in the cumulative form becomes increasingly steeper than its true model value when $N_C \lesssim 100$. To recover an accurate slope from the cumulative distribution, it must be fitted above $N_C \gtrsim 30$, whereas the differential distribution reflects the true slope down to much lower numbers per bin ($N \gtrsim 3$). Using these constraints, we fitted FLDFs of the scale-dependent distributions above their respective median $\tilde{\Lambda}_k$. For the distributions accumulated over all scales, the fitting was performed above the median value on the largest (216 $''$) scale, since this scale makes a dominant contribution to the overall shape of the accumulated distribution.

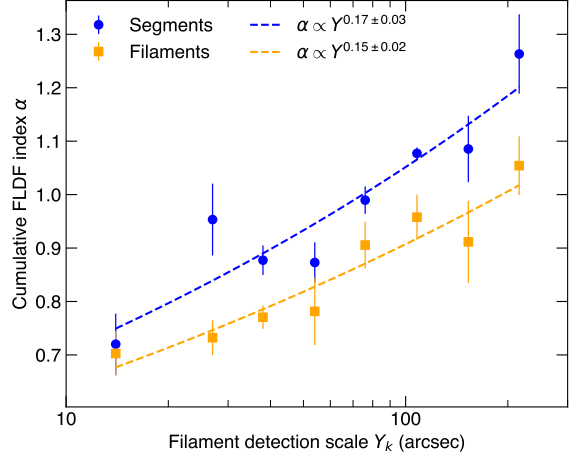


Fig. 4 Scale dependence of the filament linear density function (FLDF) index α , defined as the exponent of the power law derived from fitting the high-linear-density end of the cumulative distributions shown in the bottom row of Fig. 2. Blue circles with error bars represent measurements from filament segments, while orange squares represent measurements from whole filaments. Error bars indicate the standard error of the fitted slope in the cumulative distribution. Dashed lines show the power-law fits, with the best-fit exponents indicated.

The median values $\tilde{\Lambda}_k$ of the scale-dependent distributions combined over all clouds shift systematically from 0.70 to 9.3 $M_\odot \text{pc}^{-1}$ when the spatial scale increases from 14 to 216 $''$, following a power law $\tilde{\Lambda} \propto Y^{0.91 \pm 0.16}$. The scale-dependent FLDF slopes α_k steepen from 0.48–0.72 on the smallest scale to 1.19–1.26 on the largest scale, where the pairs of values refer to the differential and cumulative distributions. The cumulative FLDF slopes reveal a power-law scale dependence $\alpha \propto Y^{0.17 \pm 0.03}$ shown in Fig. 4.

Gravitational stability of filaments

The critical linear density $\Lambda_c = 2c_s^2/G$, where c_s is the isothermal sound speed and G is the gravitational constant, of an isothermal cylinder in hydrostatic equilibrium [19] is commonly used as a criterion to assess whether filaments are gravitationally unstable and capable of fragmenting into dense cores. For a typical dust temperature of 10 K, $\Lambda_c \approx 15 M_\odot \text{pc}^{-1}$. As discussed in [17], the applicability of this criterion to observed filaments is uncertain because the assumptions of the idealized model are generally not satisfied by the complex filaments observed in molecular clouds. We therefore adopt an uncertainty of a factor of

2 in Λ_c , defining filaments with $\Lambda < \Lambda_c/2 \approx 7.5 M_\odot \text{pc}^{-1}$ as definitively subcritical, those with $\Lambda > 2\Lambda_c \approx 30 M_\odot \text{pc}^{-1}$ as definitively supercritical, and those in between as having an ambiguous gravitational state.

Extended Data Fig. 6 shows the fractions of filament segments exceeding the three thresholds $\Lambda_c/2$, Λ_c , and $2\Lambda_c$ as functions of spatial scale for each of the seven molecular clouds. The fractions increase strongly and systematically with spatial scale for all clouds and thresholds, consistent with the near-linear scaling $\tilde{\Lambda} \propto Y$. On the smallest scales, fractions above Λ_c are near zero for most clouds, reflecting the predominantly subcritical nature of small-scale filamentary structures. On the largest scale of $216''$, fractions above the nominal threshold range from 14% in Ophiuchus to 95% in Vela C.

The cloud-to-cloud variation in supercritical fractions is substantial and broadly consistent with the known star formation activity of the clouds. When combined over all spatial scales, the fractions above the nominal threshold Λ_c range from $\sim 7\%$ in Ophiuchus and $\sim 8\%$ in Taurus to $\sim 54\%$ in Vela C, with Perseus (11%), California (12%), IC 5146 (23%), and Orion A (26%) at intermediate values.

Discussion

The composite FLDF, obtained by combining linear densities across all seven molecular clouds and all spatial scales, follows a power law $dN/d \log \Lambda \propto \Lambda^{-\alpha}$ with $\alpha \approx 1.30\text{--}1.34$, remarkably close to the Salpeter slope of 1.35 [4]. Scale-dependent slopes steepen from 0.48–0.72 on the smallest scales to 1.19–1.26 on the largest, with the Salpeter-like composite slope emerging only after integrating over the full hierarchy. This result is consistent with the single-cloud measurement of [26] for California using the same *getsf* extraction method, and extends it to a large, diverse sample. It differs from the filament linear density function reported by [18] ($\alpha \approx 1.6 \pm 0.1$ using *DisPerSe* skeletons), which we attribute to the different filament extraction method and the use of crest-averaged rather than segment-by-segment profile fitting with a novel fitting function (equation (2) in Methods).

Our measurement is the first multi-cloud, multi-scale analysis using independent filament extraction and profile fitting across the full linear density range.

The Salpeter-like slope distinguishes filaments from more diffuse molecular cloud structures, whose mass function is significantly shallower ($dN/d \log M \propto M^{-0.7}$, [30, 31]). This steepening reflects a distinct evolutionary step: starting from the shallow M^{-1} distribution expected from scale-free turbulent fragmentation [32], gravitational accretion onto supercritical filaments ($\dot{\Lambda} \propto \sqrt{\Lambda}$, [18]) naturally steepens the FLDF to the observed Salpeter value [33] on a timescale of $\sim 0.5\text{--}1$ Myr [18, 34]. The scale dependence we observe – shallower slopes on small scales, steeper on large scales – is consistent with this picture, as larger-scale filaments have had more time and mass available to accrete.

The Salpeter slope is not imprinted on any single physical scale but emerges from the statistical superposition of filamentary structures across the full range of scales. The steepening of FLDF slopes from small to large scales – from $\alpha \approx 0.5\text{--}0.7$ on the smallest scales to $\alpha \approx 1.2\text{--}1.3$ on the largest – reflects the transition from turbulence-dominated to gravity-dominated fragmentation as the spatial scale increases. We caution, however, that statistics diminish significantly toward the smallest scales, where the number of filament segments with reliable profile fits is limited; the scale-dependent steepening should therefore be treated as a trend rather than a precisely characterised relation. Previous studies emphasised a characteristic filament width of ~ 0.1 pc [11, 35], but our multiscale analysis reveals a hierarchy of widths and linear densities. Any model seeking to explain the IMF slope must account for this integrated, multiscale nature of the filamentary mass distribution.

Gravitational stability provides the physical link between the scale dependence of the FLDF and star formation activity. Since $\tilde{\Lambda} \propto Y$, larger-scale filaments are more likely to exceed the critical linear density Λ_c , and supercritical fractions increase strongly with scale for all clouds (Extended Data Fig. 6). Supercritical filaments in Vela C contain exclusively prestellar and protostellar cores [17], confirming that the largest-scale, most massive structures dominate the high- Λ tail

of the FLDF and hence the Salpeter-like composite slope. The cloud-to-cloud ordering of supercritical fractions (7–8% in Taurus and Ophiuchus to 54% in Vela C) aligns closely with independent tracers of star formation activity based on young stellar object surface densities [36, 37], while the composite FLDF slope remains close to Salpeter across all clouds – indicating an environment-independent property of the integrated filamentary mass distribution.

The FLDF can be quantitatively linked to the CMF ($dN/d\log M \propto M^{-\psi}$) through the fragmentation process. A central tenet of the filament fragmentation paradigm is that dense cores form via gravitational fragmentation of filaments [13, 20]. Consider a filament segment of length ℓ and linear density Λ : if fragmentation occurs on a characteristic length λ_{fr} , the number of cores produced is ℓ/λ_{fr} and the typical core mass is $M \sim \Lambda \lambda_{\text{fr}}$. Thus the CMF is a transformed version of the FLDF, with the transformation determined by how λ_{fr} depends on Λ . Assuming the minimal power-law parameterisation $\lambda_{\text{fr}} \propto \Lambda^\eta$, the core mass varies as $M \propto \Lambda^{1+\eta}$. Since the FLDF gives $dN/d\Lambda \propto \Lambda^{-\alpha-1}$, a standard change of variables yields the CMF slope:

$$\psi = \frac{\alpha + \eta}{1 + \eta}. \quad (1)$$

The exponent η is not a free parameter but reflects the physical regime of fragmentation. For an isothermal self-gravitating cylinder in hydrostatic equilibrium, linear perturbation theory gives the most unstable wavelength $\lambda_{\text{fr}} \propto c_s^2/(G\Lambda)$ [20], so $\lambda_{\text{fr}} \propto \Lambda^{-1}$ and $\eta = -1$: denser filaments fragment on shorter lengths. In contrast, our multiscale measurements show that median half-maximum filament widths \tilde{H} vary as $\tilde{H} \propto \tilde{\Lambda}^{0.5}$ [29]; if the fragmentation length follows the width ($\lambda_{\text{fr}} \propto H$), this implies $\eta = 0.5$, though the actual relationship between λ_{fr} and H may be more complex and the observed scaling provides only a plausible consistency check. For $\eta = 0$, the fragmentation length is independent of Λ – set for example by the sonic length or the turbulence correlation length [38, 39] – and the CMF directly inherits the FLDF slope: $\psi = \alpha$. Notably, $\eta = 0$ does not require filament widths to be constant; it only requires that the most unstable wavelength

is decoupled from Λ , which can occur when turbulence rather than gravity sets the fragmentation length. The power-law ansatz $\lambda_{\text{fr}} \propto \Lambda^\eta$ is thus a flexible description accommodating $\eta = -1$ (pure gravity), $\eta = 0$ (fixed length), and intermediate values.

The case $\eta = 0$ is consistent with the CMF in nearby clouds ($\psi \approx 1.3$ – 1.4 , [12, 16]), providing the quantitative link between the Salpeter-like FLDF and the Salpeter-like CMF; we note however that this comparison is indirect, as the FLDF and CMF are measured from different physical structures – filament segments and dense cores respectively – and a direct test requires measuring both distributions from the same clouds. We also note that the derivation assumes a roughly constant fragmentation efficiency per unit filament length; if efficiency varies with Λ , an additional factor would modify Eq. (1). Equation (1) thus provides a unified framework: the same FLDF can produce different CMF slopes depending on the dynamical environment, with η as the key empirical parameter connecting them.

The Salpeter-like FLDF slope is robust against observational biases. Because *Herschel* maps share a fixed angular resolution of $13.5''$, filaments in more distant clouds are probed at lower physical resolution, causing blending that raises their measured linear densities [29]. We tested whether blending also affects the slope by convolving each cloud’s surface density map to coarser resolutions O from 14 to $216''$ and measuring α for each resolution and each detection scale Y_k (Extended Data Fig. 7, panels (a)–(g)). Slopes show no systematic increase with O in any cloud, confirming that blending raises the measured values of linear density but does not steepen the slope. Distance-binned composite slopes (Extended Data Fig. 7, panel (h)) – $\alpha = 1.47 \pm 0.12$ for Taurus + Ophiuchus (140–144 pc), 1.38 ± 0.08 for Perseus + Orion A + California (294–470 pc), 1.29 ± 0.09 for IC 5146 + Vela C (760–920 pc), and 1.37 ± 0.08 for all distant clouds combined (294–920 pc) – are mutually consistent across a factor of ~ 7 in distance. The slight decrease in α with distance is opposite to blending-driven steepening, further ruling out an observational artifact.

Several caveats apply to the FLDF–CMF–IMF chain. The fragmentation length, core formation

efficiency, and the roles of magnetic fields and turbulence are not yet fully understood [39, 40]. The CMF–IMF mapping is not one-to-one: protostellar feedback throttles accretion [41, 42] and competitive accretion in clustered environments alters the high-mass end [43, 44]. Direct simultaneous measurements of the FLDF and CMF in the same clouds are needed.

Recent ALMA observations of high-mass protoclusters report CMF slopes substantially shallower than Salpeter. The ALMA-IMF programme finds a combined slope of $dN/d \log M \propto M^{-0.97}$ across 15 protoclusters [45]. In the framework of Eq. (1), this would require $\eta \approx 0.5$ if $\alpha \approx 1.30$ – meaning higher-density filaments fragment on longer lengths. Interestingly, our observed scaling $\tilde{H} \propto \tilde{\Lambda}^{0.5}$ [29] is consistent with $\eta \approx 0.5$ under the assumption $\lambda_{\text{fr}} \propto H$, suggesting that the shallower CMF in high-mass regions may physically reflect a width-regulated fragmentation regime. However, a hierarchical fragmentation analysis of W43-MM1 tracing the cascade from 14 kau to 270 au shows that core subfragmentation does not bring the mass function closer to Salpeter – the fragment mass function remains top-heavy ($\psi \approx 0.92$) even at disk scales [46], ruling out subfragmentation as a resolution of the discrepancy. Moreover, core masses derived from submillimetre continuum emission carry substantial systematic uncertainties from assumed dust temperatures and background subtraction that are not yet fully characterised. We therefore consider this tension unresolved: confirming whether $\eta \approx 0.5$ in high-mass regions requires direct, simultaneous FLDF and CMF measurements in the same protoclusters.

The Salpeter-like FLDF provides compelling support for a unified paradigm for the stellar IMF: (i) turbulence generates filaments with a shallow, scale-free mass distribution; (ii) gravitational accretion steepens the FLDF to the Salpeter slope; (iii) filament fragmentation with $\eta \approx 0$ produces a CMF inheriting this slope [18]; and (iv) core collapse yields the final Salpeter IMF [12]. The composite FLDF slope of 1.30–1.34 is not a coincidence: it emerges from integrating a hierarchical population of filaments whose median linear density grows linearly with spatial scale. The origin of the Salpeter slope may therefore lie in the scale-invariant properties of the filamentary mass distribution, combined with a fragmentation

length that is independent of linear density. The universality of the IMF slope is then a natural consequence not of local cloud conditions but of the global, multi-scale process of filament assembly and collapse. Equation (1) provides a quantitative tool to test and extend this picture across diverse star-forming environments: the exponent η can be empirically determined by comparing the FLDF and CMF in any cloud where both distributions are measured, directly probing how the fragmentation length depends on filament linear density.

Methods

Observational data and surface density maps

We used archival *Herschel* data¹ for seven nearby molecular clouds: Taurus, Ophiuchus, Perseus, Orion A, California, IC 5146, and Vela C. The data comprise images in five *Herschel* wavebands at 70, 160, 250, 350, and 500 μm from the HOBYS and Gould Belt surveys [1–3]. The angular resolutions of these images are 8.4, 13.5, 18.2, 24.9, and 36.3'', respectively. We resampled all images to a common 3'' pixel size using *swarp* [47]. We adopted distances of 140, 144, 294, 432, 470, 760, and 920 pc for Taurus, Ophiuchus, Perseus, Orion A, California, IC 5146, and Vela C, respectively [48, 49].

We derived H₂ surface density maps for each molecular cloud using the *hires* algorithm [27], which fits the spectral energy distribution of each pixel with a modified blackbody, assuming optically thin emission, a dust opacity law $\kappa_{\nu} \propto \nu^2$ [50, 51], and a dust-to-gas mass ratio of 0.01. Large-scale zero-level offsets were corrected by comparison with *Planck* images [52, 53]. The resulting maps have an effective angular resolution of 13.5''.

Multiscale filament extraction

Filaments were extracted with *getsf*² [27] at eight spatial scales $Y_k = 14, 27, 38, 54, 76, 108, 153,$ and 216''. We refer to quantities measured on scale Y_k with the subscript k , so that for example Λ_k

¹<http://archives.esac.esa.int/hsa/whsa/>

²<http://irfu.cea.fr/Pisp/alexander.menshchikov/>

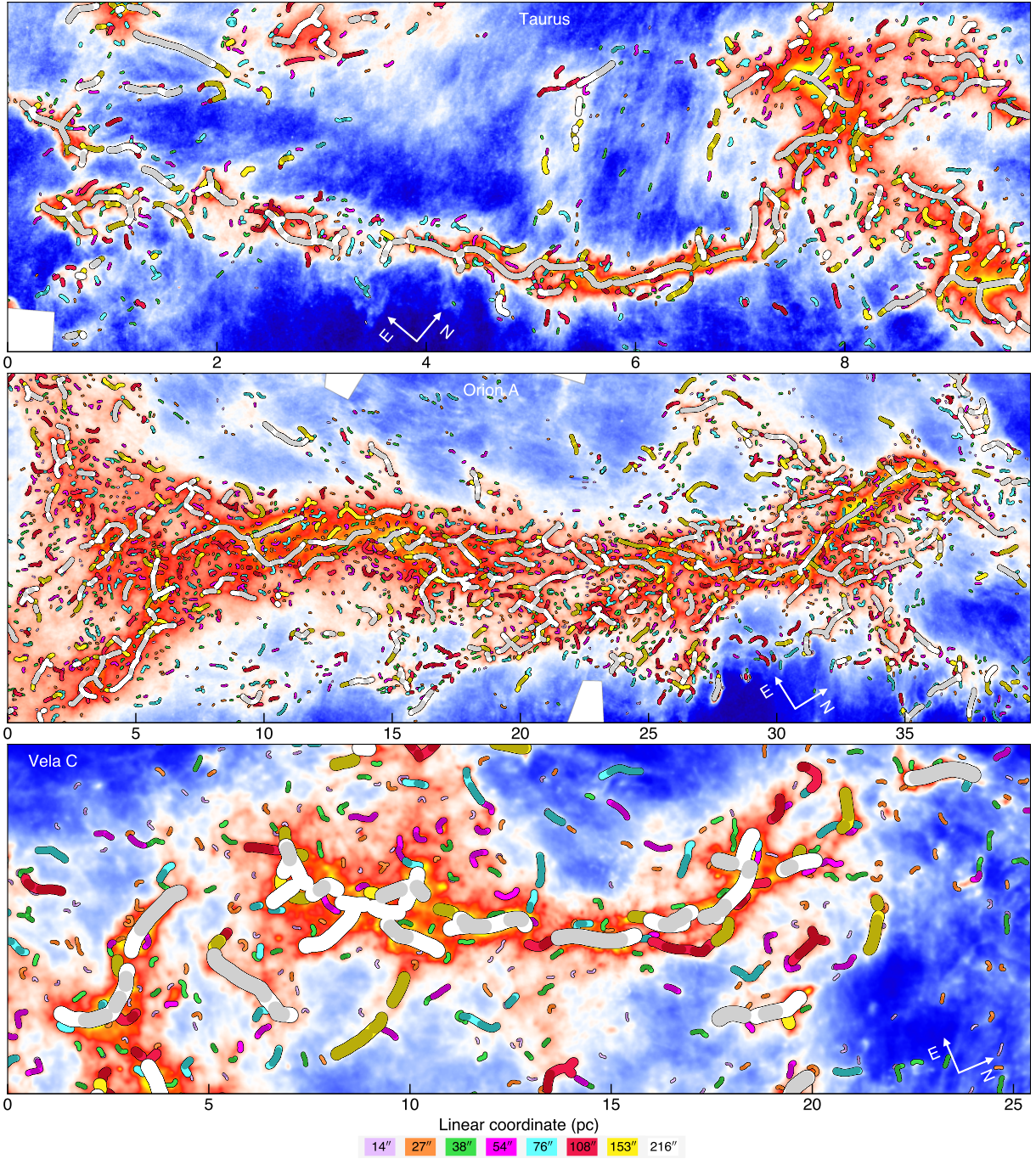


Fig. 5 Surface density images of three nearby molecular clouds – Taurus, Orion A, and Vela C – overlaid with scale-dependent filament skeletons extracted by *getsf* on spatial scales from 14 to 216". Skeleton line widths are proportional to the detection scale, as indicated in the colourbar. Darker colours denote filament segments that satisfy the profile quality criteria.

denotes the linear density measured on scale Y_k . The method decomposes images into single-scale components, removes compact sources, and traces

filament skeletons on each scale independently, ensuring that signals on scales much smaller or

larger than Y_k do not affect the skeleton derivation. The resulting skeletons uniquely represent filaments whose half-maximum widths approximately match the detection scale Y_k (Fig. 5). Skeletons were divided into 10-pixel ($30''$) segments to capture local variations in filament properties along their lengths.

Deriving linear densities from filament profiles

We applied the profile fitting method developed by [28], which accounts for the finite outer radius of filamentary structures. The surface density profile fitting function is given by

$$\Sigma(r) = \Sigma_C \left(1 + \left(2^{2/\gamma} - 1 \right) \left(\frac{2r}{w} \right)^2 \right)^{-\gamma/2} \times \left(1 - \left(\frac{r}{R} \right)^\epsilon \right)^{1/2}, \quad (2)$$

where Σ_C is the crest surface density, γ the intrinsic slope, w the intrinsic half-maximum width, R the boundary radius, and ϵ an empirical exponent ensuring consistency with the volume density profile. The fitting optimizes three independent parameters (γ , R , Σ_C); all other parameters are derived from analytical relations given in [28]. Before fitting, residual backgrounds were estimated by linear interpolation between profile endpoints and subtracted. Only profiles with coefficient of determination $R_d^2 > 0.97$, relative residuals below 0.2, and γ uncertainty below a threshold (covariance diagonal element < 2) were retained. Profiles with $\gamma = 8$ (the upper fitting bound) were excluded following [28].

The linear densities were computed by numerical integration of the fitted surface density profiles:

$$\Lambda_k = 2\mu m_H \int_0^R \Sigma_k(r) dr, \quad (3)$$

where $\mu = 2.8$ is the mean molecular weight per H_2 molecule and m_H is the mass of the hydrogen atom. Linear densities derived independently from volume density profiles agree with the surface density estimates within a median relative difference of 1% [29], confirming the robustness of the results presented here.

Power-law fitting of the FLDF

We fitted the high-linear-density tail of the differential distribution $dN/d \log \Lambda$ using logarithmic bins of width 0.2 dex, retaining only bins with $N \geq 3$. For cumulative distributions $N_C(> \Lambda)$, fits were performed for $N_C \geq 30$. For scale-dependent distributions, fitting was performed above the respective median $\tilde{\Lambda}_k$. For the distribution accumulated over all scales, fitting was performed above the median value on the largest ($216''$) scale, $\tilde{\Lambda} = 9.3 M_\odot \text{pc}^{-1}$, since this scale makes a dominant contribution to the overall shape of the accumulated distribution. This threshold is close to the critical linear density $\Lambda_c \approx 15 M_\odot \text{pc}^{-1}$ and coincides with the turnover below which the distribution flattens; fitting above different reasonable thresholds in this regime does not significantly alter the derived slopes.

Supercritical fractions

The fraction of supercritical filament segments was computed on each spatial scale Y_k for each cloud as the fraction of segments with $\Lambda_k > \Lambda_{\text{th}}$, where Λ_{th} is one of the three thresholds $\Lambda_c/2$, Λ_c , or $2\Lambda_c$, with $\Lambda_c = 15 M_\odot \text{pc}^{-1}$. Only segments meeting the profile quality criteria described above and with well-determined γ values were included. Combined fractions over all spatial scales were computed by pooling all scale-dependent measurements for each cloud.

Data availability

The *Herschel* data are publicly available from the *Herschel* Science Archive (<http://archives.esac.esa.int/hsa/whsa/>). Derived surface density maps and filament catalogs are available from the corresponding author upon request.

Code availability

The *getsf* software is available at <http://irfu.cea.fr/Pisp/alexander.menshchikov/>.

Acknowledgements

This work is based on observations obtained with *Herschel*, an ESA space observatory with science instruments provided by European-led Principal

Investigator consortia and with important participation from NASA. Images of the molecular clouds were obtained in the *Herschel* Gould Belt Survey (HGBS, PI: Ph. André), the HOBYS program (PI: F. Motte, A. Zavagno, S. Bontemps), and the A-CMC survey (PI: P. Harvey). HGBS and HOBYS are *Herschel* Key Projects jointly carried out by SPIRE Specialist Astronomy Group 3 (SAG3), scientists of several institutes in the PACS Consortium, and scientists of the *Herschel* Science Center (HSC).

This work was supported by the Key Project of International Cooperation of the Ministry of Science and Science of China through grant 2010DFA02710, and by the National Natural Science Foundation of China through grants 11503035, 11573036, 11373009, 11433008, 11403040, and 11403041. G.-Y. Zhang acknowledges support from the Postdoctoral Science Foundation of China (No. 2021T140672).

Author contributions

G.-Y. Zhang and A. Men'shchikov jointly conceived and designed the study. They performed the multiscale filament extraction, profile fitting, and analysis of the filament linear density function presented in this paper. Both interpreted the results and wrote the manuscript. J.-Z. Li participated in the scientific interpretation of the results and critically reviewed the manuscript. All authors approved the final version.

Competing interests

The authors declare no competing interests.

References

- [1] André, P. *et al.* From filamentary clouds to prestellar cores to the stellar IMF: Initial highlights from the *Herschel* Gould Belt Survey. *A&A* **518**, L102 (2010).
- [2] Motte, F. *et al.* Initial highlights of the HOBYS key program, the *Herschel* imaging survey of OB young stellar objects. *A&A* **518**, L77 (2010).
- [3] Harvey, P. M. *et al.* A First Look at the Auriga-California Giant Molecular Cloud with *Herschel* and the CSO: Census of the Young Stellar Objects and the Dense Gas. *ApJ* **764**, 133 (2013).
- [4] Salpeter, E. E. The Luminosity Function and Stellar Evolution. *ApJ* **121**, 161 (1955).
- [5] Bastian, N., Covey, K. R. & Meyer, M. R. A Universal Stellar Initial Mass Function? A Critical Look at Variations. *ARA&A* **48**, 339–389 (2010).
- [6] Offner, S. S. R. *et al.* Beuther, H., Klessen, R. S., Dullemond, C. P. & Henning, T. (eds) *The Origin and Universality of the Stellar Initial Mass Function*. (eds Beuther, H., Klessen, R. S., Dullemond, C. P. & Henning, T.) *Protostars and Planets VI*, 53–75 (2014). [arXiv:1312.5326](https://arxiv.org/abs/1312.5326).
- [7] Kroupa, P., Gjergo, E., Jerabkova, T. & Yan, Z. Mandel, I. & Schneider, F. (eds) *The initial mass function of stars*. (eds Mandel, I. & Schneider, F.) *Encyclopedia of Astrophysics, Volume 2*, Vol. 2, 173–210 (2026). [arXiv:2410.07311](https://arxiv.org/abs/2410.07311).
- [8] Kroupa, P. Grebel, E. K. & Brandner, W. (eds) *The Initial Mass Function and Its Variation (Review)*. (eds Grebel, E. K. & Brandner, W.) *Modes of Star Formation and the Origin of Field Populations*, Vol. 285 of *Astronomical Society of the Pacific Conference Series*, 86 (2002). [arXiv:astro-ph/0102155](https://arxiv.org/abs/astro-ph/0102155).
- [9] Chabrier, G. Galactic Stellar and Substellar Initial Mass Function. *PASP* **115**, 763–795 (2003).
- [10] Men'shchikov, A. *et al.* Filamentary structures and compact objects in the Aquila and Polaris clouds observed by *Herschel*. *A&A* **518**, L103 (2010).
- [11] Arzoumanian, D. *et al.* Characterizing interstellar filaments with *Herschel* in IC 5146. *A&A* **529**, L6 (2011).
- [12] Könyves, V. *et al.* A census of dense cores in the Aquila cloud complex: SPIRE/PACS observations from the *Herschel* Gould Belt

- survey. *A&A* **584**, A91 (2015).
- [13] André, P. *et al.* From Filamentary Networks to Dense Cores in Molecular Clouds: Toward a New Paradigm for Star Formation. *Protostars and Planets VI* 27–51 (2014).
- [14] Motte, F., André, P. & Neri, R. The initial conditions of star formation in the rho Ophiuchi main cloud: wide-field millimeter continuum mapping. *A&A* **336**, 150–172 (1998).
- [15] Alves, J., Lombardi, M. & Lada, C. J. The mass function of dense molecular cores and the origin of the IMF. *A&A* **462**, L17–L21 (2007).
- [16] Könyves, V. *et al.* Properties of the dense core population in Orion B as seen by the Herschel Gould Belt survey. *A&A* **635**, A34 (2020).
- [17] Li, X.-M. *et al.* Properties of the dense cores and filamentary structures in the Vela C molecular cloud. *A&A* **674**, A225 (2023).
- [18] André, P., Arzoumanian, D., Könyves, V., Shimagiri, Y. & Palmeirim, P. The role of molecular filaments in the origin of the prestellar core mass function and stellar initial mass function. *A&A* **629**, L4 (2019).
- [19] Ostriker, J. The Equilibrium of Polytropic and Isothermal Cylinders. *ApJ* **140**, 1056 (1964).
- [20] Inutsuka, S.-I. & Miyama, S. M. Self-similar Solutions and the Stability of Collapsing Isothermal Filaments. *ApJ* **388**, 392 (1992).
- [21] Zhang, G.-Y., André, P., Men'shchikov, A. & Wang, K. Fragmentation of star-forming filaments in the X-shaped nebula of the California molecular cloud. *A&A* **642**, A76 (2020).
- [22] Hacar, A., Tafalla, M., Kauffmann, J. & Kovács, A. Cores, filaments, and bundles: hierarchical core formation in the L1495/B213 Taurus region. *A&A* **554**, A55 (2013).
- [23] Hacar, A. *et al.* An ALMA study of the Orion Integral Filament. I. Evidence for narrow fibers in a massive cloud. *A&A* **610**, A77 (2018).
- [24] Fernández-López, M. *et al.* CARMA Large Area Star Formation Survey: Observational Analysis of Filaments in the Serpens South Molecular Cloud. *ApJ* **790**, L19 (2014).
- [25] Shimagiri, Y. *et al.* Probing fragmentation and velocity sub-structure in the massive NGC 6334 filament with ALMA. *A&A* **632**, A83 (2019).
- [26] Zhang, G.-Y., André, P., Men'shchikov, A. & Li, J.-Z. Probing the filamentary nature of star formation in the California giant molecular cloud. *A&A* **689**, A3 (2024).
- [27] Men'shchikov, A. Multiscale, multiwavelength extraction of sources and filaments using separation of the structural components: getsf. *A&A* **649**, A89 (2021).
- [28] Men'shchikov, A. & Zhang, G.-Y. Deriving volume density profiles of filaments from observed surface densities. *Preprint at <https://arxiv.org/abs/2604.12570>* (2026).
- [29] Zhang, G.-Y., Men'shchikov, A. & Li, J.-Z. Scale-dependent surface and volume density properties of filaments in molecular clouds. *Preprint at <https://arxiv.org/abs/2604.11485>* (2026).
- [30] Blitz, L., Levy, E. H. & Lunine, J. I. (eds) *Giant Molecular Clouds*. (eds Levy, E. H. & Lunine, J. I.) *Protostars and Planets III*, 125 (1993).
- [31] Kramer, C., Stutzki, J., Rohrig, R. & Corneliusen, U. Clump mass spectra of molecular clouds. *A&A* **329**, 249–264 (1998).
- [32] Elmegreen, B. G. The Initial Stellar Mass Function from Random Sampling in a Turbulent Fractal Cloud. *ApJ* **486**, 944–954 (1997).
- [33] Hennebelle, P. & André, P. Ion-neutral friction and accretion-driven turbulence in

- self-gravitating filaments. *A&A* **560**, A68 (2013).
- [34] Palmeirim, P. *et al.* Herschel view of the Taurus B211/3 filament and striations: evidence of filamentary growth? *A&A* **550**, A38 (2013).
- [35] Arzoumanian, D. *et al.* Characterizing the properties of nearby molecular filaments observed with Herschel. *A&A* **621**, A42 (2019).
- [36] Evans, N. J., II *et al.* The Spitzer c2d Legacy Results: Star-Formation Rates and Efficiencies; Evolution and Lifetimes. *ApJS* **181**, 321–350 (2009).
- [37] Lada, C. J., Lombardi, M. & Alves, J. F. On the Star Formation Rates in Molecular Clouds. *ApJ* **724**, 687–693 (2010).
- [38] Padoan, P. & Nordlund, Å. The Stellar Initial Mass Function from Turbulent Fragmentation. *ApJ* **576**, 870–879 (2002).
- [39] Federrath, C. On the universality of interstellar filaments: theory meets simulations and observations. *MNRAS* **457**, 375–388 (2016).
- [40] Hennebelle, P. On the origin of non-self-gravitating filaments in the ISM. *A&A* **556**, A153 (2013).
- [41] Adams, F. C. & Fatuzzo, M. A Theory of the Initial Mass Function for Star Formation in Molecular Clouds. *ApJ* **464**, 256 (1996).
- [42] Dib, S., Piau, L., Mohanty, S. & Braine, J. Star formation efficiency as a function of metallicity: from star clusters to galaxies. *MNRAS* **415**, 3439–3454 (2011).
- [43] Bonnell, I. A., Bate, M. R., Clarke, C. J. & Pringle, J. E. Competitive accretion in embedded stellar clusters. *MNRAS* **323**, 785–794 (2001).
- [44] Kroupa, P. in *Initial Conditions for Star Clusters* (eds Aarseth, S. J., Tout, C. A. & Mardling, R. A.) *The Cambridge N-Body Lectures*, Vol. 760 181 (Springer Verlag, 2008).
- [45] Louvet, F. *et al.* ALMA-IMF: XV. Core mass function in the high-mass star formation regime. *A&A* **690**, A33 (2024).
- [46] Motte, F. *et al.* (2026). Submitted.
- [47] Bertin, E. *et al.* D. A. Bohlender, D. Durand, & T. H. Handley (ed.) *The TERAPIX Pipeline*. (ed. D. A. Bohlender, D. Durand, & T. H. Handley) *Astronomical Data Analysis Software and Systems XI*, Vol. 281 of *Astronomical Society of the Pacific Conference Series*, 228 (2002).
- [48] Zucker, C. *et al.* A Large Catalog of Accurate Distances to Local Molecular Clouds: The Gaia DR2 Edition. *ApJ* **879**, 125 (2019).
- [49] Zucker, C. *et al.* A compendium of distances to molecular clouds in the Star Formation Handbook. *A&A* **633**, A51 (2020).
- [50] Hildebrand, R. H. The determination of cloud masses and dust characteristics from submillimetre thermal emission. *QJRAS* **24**, 267–282 (1983).
- [51] Ossenkopf, V. & Henning, T. Dust opacities for protostellar cores. *A&A* **291**, 943–959 (1994).
- [52] Bernard, J. P. *et al.* Dust temperature tracing the ISRF intensity in the Galaxy. *A&A* **518**, L88 (2010).
- [53] Planck Collaboration *et al.* Planck 2013 results. XI. All-sky model of thermal dust emission. *A&A* **571**, A11 (2014).

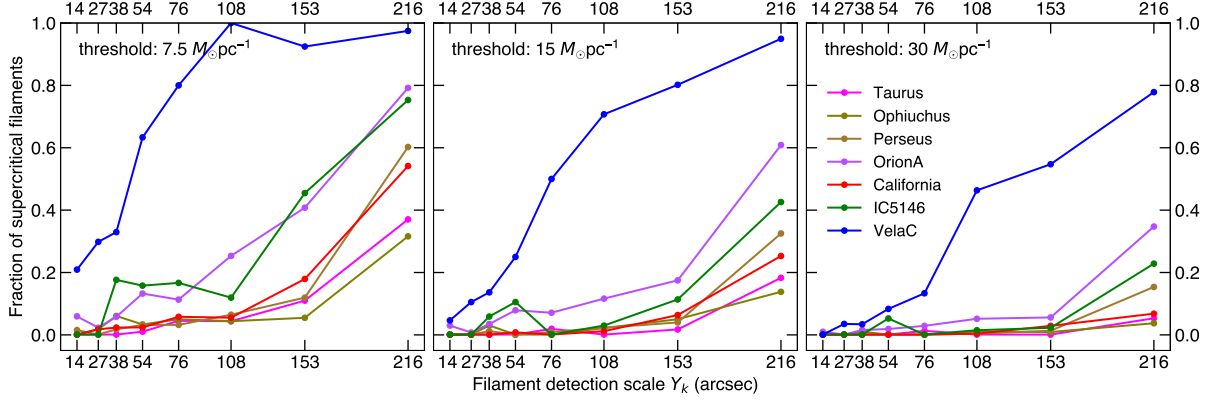


Fig. 6 Fractions of segments of filaments with supercritical linear densities as a function of spatial scale Y_k . The three thresholds $\Lambda_c/2$, Λ_c , and $2\Lambda_c$ are shown in the three panels. Coloured lines represent the seven molecular clouds. Fractions increase strongly with scale for all clouds, reflecting the near-linear scaling $\bar{\Lambda} \propto Y_k$, and span a wide range across clouds at given scale, consistent with the known variation in star formation activity.

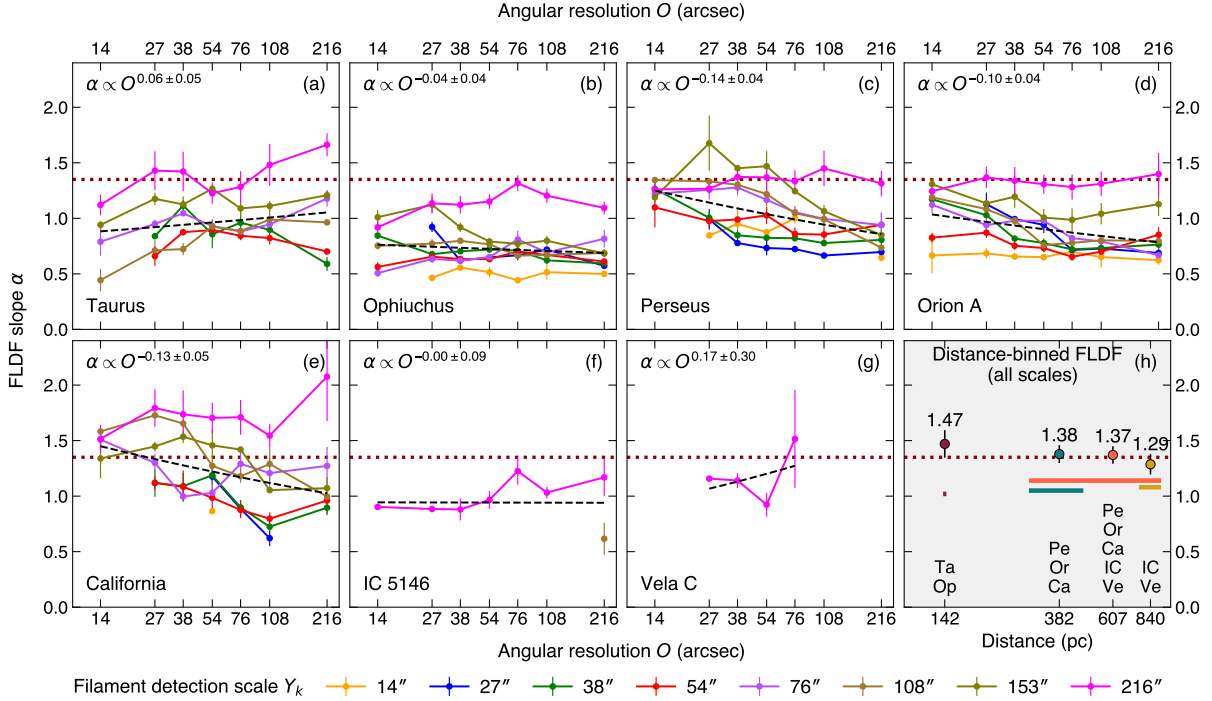


Fig. 7 Robustness of the FLDF slope against resolution degradation and distance-dependent blending. Panels (a)–(g): FLDF index α (positive, defined by $dN/d \log \Lambda \propto \Lambda^{-\alpha}$) measured from cumulative distributions as a function of angular resolution O (arcsec) for the seven molecular clouds. Different colours denote segments of filaments extracted on different detection scales Y_k (14–216"). The dotted horizontal line marks the Salpeter slope $\alpha = 1.35$ [4] for reference. The absence of a systematic increase of α with O demonstrates that the FLDF slope is not significantly steepened by changes in angular resolution, confirming that blending raises the measured values of linear density but does not steepen the power-law slope of their distribution [29]. Panel (h): Composite FLDF slopes obtained by combining all spatial scales for distance-binned cloud sub-samples: Ta+Op (Taurus + Ophiuchus, 140–144 pc), Pe+Or+Ca (Perseus + Orion A + California, 294–470 pc), IC+Ve (IC 5146 + Vela C, 760–920 pc), and the full distant sample Pe+Or+Ca+IC+Ve (294–920 pc). Data points are placed at the median distance of each group; horizontal bars of the same colour indicate the corresponding distance range and are offset vertically to avoid overlap. Error bars are standard errors from power-law fits to the cumulative distributions. All composite slopes are mutually consistent and close to $\alpha = 1.35$ [4], confirming that the Salpeter-like FLDF is a robust feature independent of cloud distance and blending.